

**Title: Computational modelling of ovine critical-sized tibial defects with implanted scaffolds and prediction of the safety of fixator removal.**

**Author Names:** Heather Doyle<sup>a</sup>, Stefan Lohfeld<sup>a</sup>, Lutz Dürselen<sup>b</sup>, Peter McHugh<sup>a</sup>

**Author Affiliations:**

<sup>a</sup>Biomechanics Research Centre (BMEC), Biomedical Engineering, National University of Ireland, Galway, Ireland.

<sup>b</sup>Institute of Orthopaedic Research and Biomechanics Centre of Musculoskeletal Research, University of Ulm, Ulm, Germany

**Corresponding Author:** Heather Doyle

Email: [heatherdoylenuig@gmail.com](mailto:heatherdoylenuig@gmail.com)

---

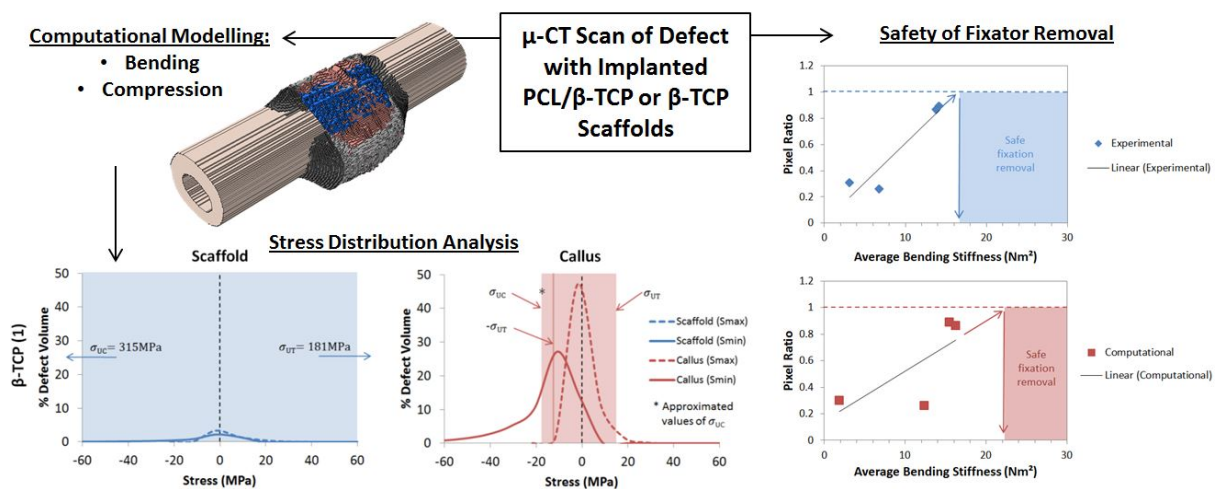
Accepted manuscript. Published version: <http://dx.doi.org/10.1016/j.jmbbm.2015.01.008>



© 2015. This manuscript version is made available under the CC-BY-NC-ND 4.0 license <http://creativecommons.org/licenses/by-nc-nd/4.0/>

# 1 Abstract

Computational model geometries of tibial defects with two types of implanted tissue engineering scaffolds,  $\beta$ -tricalcium phosphate ( $\beta$ -TCP) and poly- $\epsilon$ -caprolactone (PCL)/ $\beta$ -TCP, are constructed from  $\mu$ -CT scan images of the real *in vivo* defects. Simulations of each defect under four-point bending and under simulated *in vivo* axial compressive loading are performed. The mechanical stability of each defect is analysed using stress distribution analysis. The results of this analysis highlights the influence of callus volume, and both scaffold volume and stiffness, on the load-bearing abilities of these defects. Clinically-used image-based methods to predict the safety of removing external fixation are evaluated for each defect. Comparison of these measures with the results of computational analyses indicates that care must be taken in the interpretation of these measures.



## 2 Introduction

Stabilisation of critical-sized defects in long bones is a major challenge in bone tissue engineering. A critical-sized defect is a large defect in a bone that will not heal on its own without intervention. It is widely understood that while often effective, donor site morbidity is an issue with the use of autografts in treating this type of defect due to the volume of tissue required. Bone tissue engineering scaffolds have been developed from a wide range of materials to address this challenge [1–6]. External fixation of the bone is generally required for stabilisation of critical-sized defects during the early stages of healing until sufficient mechanical integrity has been achieved. Quantifying the degree of healing and mechanical integrity required for fixation removal is important as “leaving the apparatus on for longer than necessary is as harmful as removing the fixator too early” [7].

Investigations of fracture callus mechanical integrity under uniaxial loading [8–10], bending loading [11] and analysis of the transmission of *in-vivo* loading through a tibial fracture callus [12] have been carried out using anatomically accurate finite element (FE) models generated from micro-computed tomography ( $\mu$ -CT) scans. Similar methods were employed by Roshan-Ghias et al. [13] to generate FE models of a scaffold-callus construct for uniaxial loading simulations. The use of four-point bending tests gives a more complete picture of the mechanical integrity of the scaffold-callus construct [6,11] under the complex loading conditions *in-vivo* [14] in comparison to the use of uniaxial loading alone.

*In-vivo* studies using nanoindentation have shown that fracture callus stiffens over time as mineralisation increases [15,16], therefore the mechanical properties used in FE models must be representative of the callus stiffness at the appropriate stage in healing and mineralisation. When appropriate, experimentally-obtained mechanical properties of the actual tissues being

modelled should be used; however, when building models using non-invasive techniques this is not always feasible. In some cases, data from relevant literature can be sufficient when care is taken to interpret experimental [12,17].

Non-invasive methods to quantify bone formation within a defect site based on imaging method such as X-ray and  $\mu$ -CT have been developed in order to provide clinicians with a means to make informed decisions regarding the removal of external fixation. The most common clinically-used criterion for the removal of fixation is the measurement of the thickness of continuous cortices of bone bridging a defect using X-rays, with reported re-fracture rates of 4% [18] and 3% [19]. A pixel value ratio ( $P_r$ ), evaluated from X-ray images, has also been used as a guide for fixation removal, with re-fractures reported in defects with  $P_r < 0.8$  [20] and a suggested optimal  $P_r$  value of 1 [21]. The 2D nature of these quantitative callus assessment methods is a limiting factor as they do not account for 3D variations in callus density or continuous loading paths of bone. Other measurements such as bone mineral density, a scalar value from a DEXA scan [22,23], and a strength–strain index ( $SSI$ ), defined as the cross-sectional moment of inertia ( $CSMI$ ) weighted by density distribution [24,25], and  $CSMI$  [26] have also been identified as useful measures of callus integrity.  $CSMI$  was found to have high correlation with bending breaking force determined using three-point bending [26]. While a more complete picture of overall callus mechanical integrity is achieved using these 3D measures ( $P_r$  and  $CSMI$ ) in comparison to the 2D methods above, the presence of continuous loading paths within the bone callus is still not accounted for.

Against this backdrop the overall aim of the present work is to investigate the mechanical stability of critical-sized tibial defects with implanted scaffolds and a bony callus, using FE modelling in conjunction with experimental test results. Specifically, the first objective of the study is to generate detailed FE models of real defect geometries using  $\mu$ -CT scans, and to

verify the accuracy of the models against experimental data [6]. The second objective is to use the developed FE models to explain the experimentally observed mechanical performance of these defects, and to evaluate the safety of removing the fracture fixation device in each case. The third objective is to compare the performance of the FE models and the performance of two other clinically-used callus-evaluation parameters,  $P_r$  (2D) and  $CSMI$  (3D), as non-invasive methods to predict safe fixation removal, for the defects of interest here, and to draw conclusions on their respective suitability. A flowchart outlining the individual steps taken to generate the models and address the objectives in the present study is shown in Figure 1.

## 3 Methods

### 3.1 *In Vivo* Study Data

This study is based around an *in vivo* study of two types of scaffolds implanted in critical-sized ovine tibial defects as part of the STEPS EU-FP6 project [6] (Figure 2(A)): 90/10wt% PCL/ $\beta$ -TCP scaffolds fabricated using selective laser sintering and commercially available  $\beta$ -TCP scaffolds (Biovision, Illmenau, Germany). Defects were stabilised using a titanium plate and fixation screws and defect imaging was carried out at 14 weeks post-operative using a  $\mu$ -CT scanner (Fan Beam  $\mu$ -Scope, Stratec, Pforzheim, Germany) and X-ray. Four-point bend testing was carried out on both left and right tibiae (at 14 weeks), as per Figure 3(A), to a maximum load of 40 N. In each case, the right tibiae were operated on and the left tibia was left intact. Each tibia was rotated in 30° increments about the longitudinal axis to determine the bending stiffness in 360° [6]. Four defect cases/specimens were selected for study here;

two with implanted PCL/ $\beta$ -TCP scaffolds and two with  $\beta$ -TCP scaffolds. The equivalent bending stiffness,  $K_B$ , was calculated using Equation (1) [27]:

$$K_B = \frac{(2b + 3a)b^2k}{12} \quad (1)$$

where  $b$  is the unsupported length between the two outermost supports,  $a$  is the distance between the loading supports and  $k$  is the slope of the load-deflection curve, as indicated in Figure 3. From the experimental data, twelve values of bending stiffness,  $K_B^{Exp}$ , (i.e.  $0^\circ$  -  $360^\circ$ , in  $30^\circ$  increments) were calculated for each of the four samples, and an average value determined for each sample. A  $\mu$ -CT scan of an intact, undegraded PCL/ $\beta$ -TCP scaffold, from the same build as the scaffolds used in the *in vivo* study, was also obtained for the purposes of this study using a Skyscan 1172 (Skyscan B.V., Kontich, Belgium)  $\mu$ -CT scanner at the University of Ulm, Germany.

### 3.2 Generation of Model Geometries

FE models of the tibial defect were constructed from  $\mu$ -CT scans of each defect volume that were obtained following the termination of the *in vivo* study. The model assembly process is outlined in Figure 1. Each of the four full models consists of the real bony callus tissue geometry, the implanted tissue engineering scaffold, the tibia and soft tissue. Individual model “parts” for the callus region and the scaffold were generated from  $\mu$ -CT scans using MIMICS software (Materialise, Belgium), and are described in detail below. Additionally, idealised part geometries were generated using MIMICS for the regions of the callus outside of the  $\mu$ -CT scan volume, for the tibia (with constant cross-section and a length of 80 mm) and for soft tissue based on the available  $\mu$ -CT scans and X-ray images.

For the defects with implanted  $\beta$ -TCP scaffolds, both scaffold and callus have similar grey-values and are visible in the  $\mu$ -CT scans, as shown in Figure 2(B) and model geometries for each of these parts were generated directly from the  $\mu$ -CT scans using MIMICS. The callus tissue geometry was generated by segmenting tissue with grey-values ranging from 40 to 90 and was separated into five separate parts based on grey-value to account for material property heterogeneity. For the defects with implanted PCL/ $\beta$ -TCP scaffolds, the callus tissue geometry was generated by segmenting tissue with grey-values ranging from 40 to 180, based on visible tissue regions. Similar to the  $\beta$ -TCP scaffold case, callus regions were separated into five separate parts to represent five ranges of grey-value. As the PCL/ $\beta$ -TCP scaffold geometry is not visible in the  $\mu$ -CT scans due to differences between scaffold and callus grey-values, (see Figure 2(B)), the scaffold geometry was obtained from a separate scan and was imported and aligned within each defect using MIMICS. Any scaffold material intersecting the surrounding bone callus region was removed using Boolean subtraction.

Full model geometries were assembled using the merge mesh tool in Abaqus/CAE, as illustrated in Figure 4, and outlined in Figure 1. Each of the four assembled model geometries, i.e. two assembly models for each scaffold type, was assigned a label ( $\beta$ -TCP (1),  $\beta$ -TCP (2), PCL/ $\beta$ -TCP (1) and PCL/ $\beta$ -TCP (2)). Infinitesimal deformation kinematics was assumed (NLGEOM turned off) to simplify the simulations, within Abaqus/Standard.

### **3.3 Four-Point Bending Test Model Development**

Simulations of four-point bending were carried out to assess the bending stiffness of both intact tibiae and tibial defects with implanted scaffolds, as outlined in Figure 1. The computational model implementation is illustrated in Figure 3(B); the tibia was positioned such that the centroid of the tibial cross-section lies at zero on both the 1- and 2-axis, and that

the longitudinal axis is aligned with the 3-axis (see Figure 3(B)). The mid-point of the tibia was positioned at  $x_3 = 0$ , leaving a 40 mm length at either side. Reference Points (RPs) for boundary conditions were positioned at (0, 0, 80) and (0, 0, -80), giving an unsupported span of 60 mm at each end. Boundary conditions were applied to each RP to restrict motion to rotation about the 1-axis. Each end of the tibia was constrained to the closest RP using multi-point constraints (specifically, \*MPC Beam constraints). A loading node was selected from the top layer of nodes at both  $x_3 = 20$  mm and at  $x_3 = -20$  mm to give a loading span of 40 mm. \*MPC Tie constraints were created between each loading node and the remaining nodes at the top surface at the same  $x_3$ -position. A force of 20 N was applied to each loading node with a smooth step amplitude (load = 0 N at step time = 0, load = 20 N at step time = 1). The average displacement at the loaded nodes was recorded and the slope of the load-deflection curve ( $k$ ) was calculated. From this the bending stiffness was calculated using Equation (1). To mimic the experiments, each model was rotated in  $30^\circ$  increments about the longitudinal axis and  $K_B^{Comp}$  was evaluated for each increment. An average value was also generated for each of the four models ( $n = 12$ ). The statistical difference between the experimental bending stiffness values,  $K_B^{Exp}$ , and computational bending stiffness values,  $K_B^{Comp}$ , was evaluated for each model using an unpaired T-test ( $n = 12$ ).

### **3.4 Elastic Property Assignment**

The elastic properties for the various material components in the FE models, specific to the specimens used in this study, are summarised in Table 1. Linear elastic properties were assumed for all materials.

The value of ovine cortical bone elastic modulus (11 GPa) was established using an iterative process involving four-point bending FE simulations, using models of the intact tibia alone

(i.e. no defect and scaffold present). Data for the experimentally-evaluated bending stiffness of intact tibiae that was generated as part of the STEPS project [6].

A relationship between the mechanical properties of SLS fabricated scaffolds and grey-value has previously been demonstrated [28]. In order to account for this, the elastic modulus of the undegraded PCL/ $\beta$ -TCP scaffolds was approximated based on the grey-value, using the method and data that were presented in previous studies [29,30], giving a value of 250.37 MPa. The elastic modulus of the PCL/ $\beta$ -TCP scaffold materials after an equivalent of 14 weeks simulated ageing, evaluated in a previous study [31], was 37.43% of the original value, therefore a value of degraded scaffold elastic modulus can be approximated as 93.71 MPa. Bending test simulations were carried out using both undegraded and degraded values for PCL/ $\beta$ -TCP scaffold elastic modulus.

The overall range of grey-values is greater in the PCL/ $\beta$ -TCP defect scans than in the  $\beta$ -TCP defect scans (due to differences in scan settings); therefore the appropriate values of  $E_{\text{callus}}$  in models of defects with PCL/ $\beta$ -TCP scaffolds were calculated using a scaling factor ( $s$ ), which was calculated based on cortical bone grey-value. Average values of cortical bone grey-value were calculated for defects with  $\beta$ -TCP scaffolds (84.49) and PCL/ $\beta$ -TCP scaffolds (134.03), giving  $s = 84.49 / 134.03 = 0.63$ .

### **3.5 Compressive Loading**

Compression simulations to replicate the axial loading experienced by the scaffold-callus construct *in vivo* were carried out to give a snapshot of the load-bearing abilities of each individual defect at 14 weeks post-implantation, as outlined in Figure 1. Peak axial tibio-femoral contact forces in sheep of 2.12 x body weight were recorded by Taylor et al. [14], and an average body weight for sheep of 647.5 N can be calculated from values reported by

Bergmann et al. [32]. The axial contact force,  $F$ , can then be calculated giving  $F = 2.12 \times 647.5 = 1.3727$  kN. Compression simulations were carried out using the model geometries described in Section 3.2 where a constant, compressive force of 1.3727 kN was applied to one end of the tibia. The displacements of all nodes on this end of the tibia were constrained to a loading node in the 3-direction using a \*EQUATION constraint. The displacements of nodes on the opposite end of the tibia were fixed in the 3-direction, with one node fixed in all directions.

### 3.6 Stress Distribution Analysis

The maximum stress failure criterion was used to assess the failure of materials in each simulation, as outlined in Figure 1. The maximum stress failure criterion assumes that failure will occur when the maximum principal stress ( $\sigma_{Max}$ ) in a material exceeds the ultimate tensile strength ( $\sigma_{UT}$ ) of the material, or when the minimum principal stress ( $\sigma_{Min}$ ) is less than the ultimate compressive strength ( $\sigma_{UC}$ ) of the material. The safe region for the material is then described as:

$$\sigma_{UC} < \sigma_{Min} < \sigma_{Max} < \sigma_{UT} \quad (2)$$

The values of  $\sigma_{UT}$  and  $\sigma_{UC}$  for each material that are used in this study are summarised in Table 2. The principal stress distribution in each part was analysed using a script written in Matlab (Mathworks, UK). The total range of stress values in each model was divided into sub-ranges (increments of 1 MPa for bending simulations, 10 MPa for compression simulations) and the number of elements with stress values within each range was calculated. The percentage of elements in which material failure is predicted to occur, i.e. the percentage

of elements outside of the safe zone according to Equation (2), was calculated, and was normalised by the total defect volume (callus, scaffold and soft tissue).

### 3.7 Callus Assessment Measurements

Two types of callus assessment measurements are calculated for each individual defect to evaluate the risk of removing external fixation at this point in time (14 weeks post implantation), as outlined in Figure 1. The pixel value ratio ( $P_r$ ) [22] for each individual defect was calculated using Equation (3). Mean pixel value was evaluated from X-ray images of each defect at 14 weeks *in vivo* using MIMICS, as illustrated in Figure 5. The mean pixel value was calculated for three regions on each X-ray image: within the bone callus, above the bone callus and below the bone callus (Figure 5). The mean pixel value of intact bone was taken to be the average of pixel values calculated above and below the defect.

$$P_r = \frac{\text{mean pixel value of callus bone}}{\text{mean pixel value of intact bone (distal and proximal)}} \quad (3)$$

The cross-sectional moment of inertia ( $CSMI$ ) of each individual defect was calculated using Equation (4), where  $a_i$  is the area of one voxel and  $(y_i - y_c)$  is the distance from a voxel ( $i$ ) to the central axis ( $y_c$ ). The BoneJ plugin for ImageJ software was used to calculate the value of  $CSMI$  in the 3-direction for each defect from  $\mu$ -CT scans.

$$CSMI = \sum a_i (y_i - y_c)^2 \quad (4)$$

## 4 Results

### 4.1 Four-Point Bending Simulations

Four-point bending simulations of computational model geometries of tibiae with defects containing  $\beta$ -TCP scaffolds and PCL/ $\beta$ -TCP scaffolds were carried out to generate a full set of  $K_B^{Comp}$  data, which is shown in comparison to experimental data [6] in Figure 6. No significant difference between  $K_B^{Exp}$  and  $K_B^{Comp}$  was found for defects with the  $\beta$ -TCP scaffolds, with P values of 0.16 and 0.46 for  $\beta$ -TCP (1) and  $\beta$ -TCP (2), respectively (n = 12) showing a good fit between experimental and computational measurements of bending stiffness. Significant differences between  $K_B^{Exp}$  and  $K_B^{Comp}$  were found with P values of 0.002 and 0.0001 for PCL/ $\beta$ -TCP (1) and PCL/ $\beta$ -TCP (2), respectively (n = 12). The use of degraded elastic modulus values for PCL/ $\beta$ -TCP scaffolds resulted in a 3% reduction in bending stiffness for PCL/ $\beta$ -TCP (1) and a 39.3% reduction for PCL/ $\beta$ -TCP (2), as shown in Figure 6.

### 4.2 Stress Distribution Analysis

The principal stress distribution for four-point bending simulations is shown in Figure 7, and for compressive loading in Figure 8. In each plot, shaded regions represent the safe regions, with stresses between  $\sigma_{UC}$  and  $\sigma_{UT}$ , in red for the callus region and blue for each scaffold type. Approximated values of  $\sigma_{UC}$  are indicated with an asterisk, and  $-\sigma_{UT}$  values for both scaffold and callus are included as solid lines to indicate conservative values of  $\sigma_U$ . Elements with stresses outside these limits indicate predicted material failure. In such cases the volume of predicted failed callus or scaffold material can be determined from the plots as the area

under the respective curve outside the safe region, in terms of a percentage of total defect volume, and the relevant values are reported below.

Under bending loading (Figure 7), failure is predicted in less than 0.01% volume, for the scaffold and callus parts, for models  $\beta$ -TCP (1),  $\beta$ -TCP (2) and PCL/ $\beta$ -TCP (1). The greatest volume of failed material under bending loading occurs in the PCL/ $\beta$ -TCP (2) model, with failure in compression (failed volume of 0.1%) and failure in tension (failed volume of 21%) predicted in the scaffold part.

The magnitudes of stress are greater in the compression simulations (Figure 8) than in the bending simulations. Failure in compression is predicted in a greater volume of the callus tissues in defects with  $\beta$ -TCP scaffolds (failed volumes of 22% and 15% for  $\beta$ -TCP (1) and  $\beta$ -TCP (2), respectively) than in defects with PCL/ $\beta$ -TCP scaffolds (failed volumes of 4% and 5% for PCL/ $\beta$ -TCP (1) and PCL/ $\beta$ -TCP (2), respectively). Similar results were observed for predicted failure in tension, with failed volume values of 6%, 0.5%, 0.08% and 0.34% for  $\beta$ -TCP (1),  $\beta$ -TCP (2), PCL/ $\beta$ -TCP (1) and PCL/ $\beta$ -TCP (2), respectively. The opposite result was found in the case of the scaffold materials, with compressive failure only predicted for the PCL/ $\beta$ -TCP (2) model. No tensile failure was predicted within either  $\beta$ -TCP scaffold volume, however tensile failure is predicted in 1.6% and 18.3% of the scaffold volume in models PCL/ $\beta$ -TCP (1) and PCL/ $\beta$ -TCP (2), respectively.

### **4.3 Callus Assessment Methods**

The values of  $K_B$  for each defect are compared with the calculated values of  $P_r$  to generate threshold values of  $K_B$  for safe fixation removal. The value of  $P_r$  for each defect is shown with respect to the average values of  $K_B^{Exp}$  and  $K_B^{Comp}$  in Figure 9.  $P_r$  is a better predictor of

average  $K_B^{Exp}$  ( $r = 0.95$ ) than of average  $K_B^{Comp}$  ( $r = 0.72$ ). Using a linear fit between bending stiffness and  $P_r$ , the value of  $K_B$  corresponding to a  $P_r$  of 1 was calculated, giving threshold bending stiffness values of 16.5 Nm<sup>2</sup> and 22.7 Nm<sup>2</sup> for experimental and computational results respectively.  $CSMI$  is shown with respect to  $K_B^{Exp}$  and  $K_B^{Comp}$  in Figure 10.  $CSMI$  is a better predictor of  $K_B^{Exp}$  ( $r = 0.92$ ) than of  $K_B^{Comp}$  ( $r = 0.82$ ). Using a linear fit between bending stiffness and  $CSMI$ , the predicted threshold values of  $CSMI$  for fixation removal, corresponding to  $K_B$  values of 16.5 Nm<sup>2</sup> and 22.7 Nm<sup>2</sup>, were calculated. In this way, threshold values of  $CSMI$  of  $334 \times 10^9$  kg.mm<sup>2</sup> and  $353 \times 10^9$  kg.mm<sup>2</sup> were calculated for experimental and computational results, respectively. In comparison to the experiments, the models generate a higher bending stiffness threshold (to ensure that  $P_r > 1$ ), i.e. a more conservative bending stiffness threshold for fixation removal.

## 5 Discussion

FE model geometries for tibiae with implanted scaffolds and new bone callus geometries were generated from the defect region  $\mu$ -CT scan images. The model generation process was simpler, and more accurate, for defects with implanted  $\beta$ -TCP scaffolds than for defects with PCL/ $\beta$ -TCP scaffolds as the geometry of both scaffold and bone callus were visible on the same scan images (Figure 2(B)). In cases where the scaffold is not visible in  $\mu$ -CT scans, the real scaffold geometry should be obtained using a secondary scan at settings optimal for the scaffold material. The four-point bending simulations accurately predict tibial bending stiffness for defects with implanted  $\beta$ -TCP scaffolds, verifying the material properties used in these simulations. For defects with implanted PCL/ $\beta$ -TCP scaffolds, the relative trend of

bending stiffness is preserved and the models give a reasonable estimate of tibial bending stiffness, achieving the first objective of this study. The effect of decreasing scaffold stiffness, due to degradation, resulted in a greater reduction in overall defect stiffness in the PCL/ $\beta$ -TCP (2) model, in which the callus volume is 3.5 times smaller than in than the PCL/ $\beta$ -TCP (1) model. This demonstrates then that the callus volume strongly influences the overall stiffness of the scaffold/callus construct.

The evaluation of stress distribution under bending loading (Figure 7) gives a useful insight into load distribution within each individual defect. The primary load-bearing component in the case of defects with  $\beta$ -TCP scaffolds is the callus tissue, whereas load-bearing is shared between the scaffold and callus in PCL/ $\beta$ -TCP (1). The primary load-bearing component in PCL/ $\beta$ -TCP (2) is the scaffold and the volume of callus tissue is 3.5 times less than in PCL/ $\beta$ -TCP (1). Failure was not predicted in any of the four cases under bending loading; this is consistent with the observations of experimental bending testing where failure did not occur during repeated bending loading of the samples [6]. This essentially serves as a validation of the models and the choice of material property values presented here.

Analysis of the stress distribution in each defect under compressive loading (Figure 8) shows similar results to Figure 7 in terms of the load-bearing component in each model. The primary load-bearing component in  $\beta$ -TCP (1) is the callus tissue, whereas load-bearing is shared between the scaffold and callus in  $\beta$ -TCP (2) and in PCL/ $\beta$ -TCP (1) and the primary load-bearing component in PCL/ $\beta$ -TCP (2) is the scaffold. Under both loading types, the callus is the load-bearing component in cases with a sufficiently large callus volume.

The results of the stress distribution analysis under both loading types are consistent with the results of mechanical testing of the defects, as presented in Lohfeld et al. [6] and in Figure 5.

Defects with implanted  $\beta$ -TCP scaffolds are shown to have greater bending stiffness compared to defects with implanted PCL/ $\beta$ -TCP scaffolds [6]. The results presented here predict that loading is supported primarily by the callus volume in each of the  $\beta$ -TCP scaffold cases, compared to a shift towards loading being supported by the scaffold in the PCL/ $\beta$ -TCP scaffold cases. This is to be expected from the high volume of mineralised callus tissue in the  $\beta$ -TCP cases relative to the PCL/ $\beta$ -TCP cases [6], and these results indicate that the scaffold plays a mechanical support role when low callus volumes are present.

The percentage volume of material within each defect in which failure is predicted under *in vivo* compressive loading is worthy of note. For defects with the  $\beta$ -TCP scaffolds, failure is predicted in volumes of 26.2% and 15% (tension and compression, respectively) of the callus tissues and no failure of the scaffold material is predicted. In contrast, failed volumes of 3.9% and 5% (tension and compression, respectively) are predicted in the callus region in defects with PCL/ $\beta$ -TCP scaffolds along with failed volumes of 1.6% and 19.2% (tension and compression, respectively) in the PCL/ $\beta$ -TCP scaffolds themselves. These results indicate that the magnitudes of loading that are estimated to be experienced *in vivo* in sheep tibiae during normal gait would result in failure of the tibia-callus-scaffold assembly, and that removal of external fixation at this time (14 weeks) would be premature. These results fulfil the goals of the second objective of this study to evaluate the safety of removing the fracture fixation device in each case.

The clinical measures of parameters,  $P_r$  and  $CSMI$ , have been evaluated for each individual defect (Figure 9 and Figure 10) to meet the third objective of this study.  $P_r$  is the ratio of the mean callus pixel value to the mean intact bone pixel value, and  $CSMI$  is the cross-sectional moment of inertia of each individual defect. Using the suggested threshold of  $P_r = 1$  for the

safe removal of external fixation [21], none of the four defects studied here qualify for removal of external fixation. It is interesting to note that threshold values of each measure ( $P_r$  and  $CSMI$ ) that have been calculated to predict the safe removal of fixation are not significantly greater than the predicted values for defects with  $\beta$ -TCP scaffolds (0.89 and 0.86). This suggests that these defects are relatively close to what would be considered full healing by these measurements and is somewhat surprising given that these defects are not capable of supporting *in vivo* compressive loading, according to the results of the *in vivo* compressive loading simulations and stress distribution analysis (Figure 8) presented here. This indicates that the threshold levels of bone formation required for fixation removal are underestimated by  $P_r$ , leading to the calculation of a non-conservative threshold value of  $CSMI$ . Increased volume and stiffness of callus tissue or reduced scaffold degradation would be required for safe fixation removal in the case of these specific defects. These results suggest that the use of these measures ( $P_r$  and  $CSMI$ ) may need to be treated carefully, as the results call into question how appropriate they are as predictors for safe fixation removal. It is accepted that the compression simulations presented here are not directly supported by experimental testing, however the results presented here do point to the need for experimentation to explore the issue further. It should be noted that both  $P_r$  and  $CSMI$  are evaluated directly from X-ray and  $\mu$ -CT scan images in which the PCL/ $\beta$ -TCP scaffolds are not visible, therefore the contribution of the scaffold to the load-bearing abilities of the scaffold-callus construct are not accounted for by either method; this limitation affects the accuracy of these evaluation methods for the case of these specific defects.

A major advantage of the FE-based methods that are presented here is that a non-invasive method to assess the mechanical integrity of the scaffold-callus construct is provided. This can be combined with repeated  $\mu$ -CT scanning during longitudinal *in vivo* studies to assess

the development of a new bone callus and its contribution to the overall mechanical performance of the scaffold-callus construct. The results presented above, for defects with  $\beta$ -TCP scaffolds in particular, demonstrate that generic material properties from the literature can be used in anatomically accurate models to accurately predict bending stiffness when carefully calibrated as in this study. The load-bearing abilities of the defect can be evaluated using failure criteria, and the safety of removing external fixation can be evaluated. The models that are generated are also anatomically accurate and defect-specific, or patient-specific, and provide individualised information for live subjects for the clinician that would otherwise be unavailable.

## **6 Conclusions**

The mechanical integrity of defects with two types of implanted scaffold,  $\beta$ -TCP and PCL/ $\beta$ -TCP, was analysed using computational simulations of both bending and compression loading and stress distribution analysis. The results of these analyses indicate that fixation removal would be premature and highlight the influence of callus volume and scaffold volume on the load-bearing abilities of these defects. Clinically-used measures to predict the safety of removing external fixation also predict that removal of external fixation would be premature; however the results of this study indicate that care must be taken in the interpretation of these measures.

The methods presented here have potential for the development of a non-invasive computational assessment of defect stability. Analysis of the scaffold-callus construct at successive time-points during the course of fracture callus healing would provide insight into

the transfer of load-bearing from scaffold to callus as scaffold degradation increases and as callus formation progresses and mineralisation increases. The load-bearing abilities of the entire defect (callus and scaffold) as healing progresses can be assessed using both bending and compression loading simulations and compared with clinically-used measurements to evaluate the suitability of fixation removal. In this way, patient-specific computational modelling can inform decision making in a clinical setting by providing additional information about the load-bearing abilities of any defect at a given point in time.

## **7 Acknowledgements**

H. Doyle acknowledges funding from the Irish Research Council under the Embark Initiative Postgraduate Research Scholarship Scheme, and the SFI/HEA Irish Centre for High-End Computing (ICHEC) for the provision of computational facilities and support. The authors acknowledge research funding from the European Union through the STEPS FP6 project (contract number FP6-500465) and also the partners in the STEPS project for their input.

## 8 References

- [1] Bhumiratana S, Grayson WL, Castaneda A, Rockwood DN, Gil ES, Kaplan DL, et al. Nucleation and growth of mineralized bone matrix on silk-hydroxyapatite composite scaffolds. *Biomaterials* 2011;32:2812–20. doi:10.1016/j.biomaterials.2010.12.058.
- [2] Lee SJ, Lim GJ, Lee J-W, Atala A, Yoo JJ. In vitro evaluation of a poly(lactide-co-glycolide)-collagen composite scaffold for bone regeneration. *Biomaterials* 2006;27:3466–72. doi:10.1016/j.biomaterials.2006.01.059.
- [3] Yao D, Smith A, Nagarajan P, Vasquez A, Dang L, Chaudhry GR. Fabrication of polycaprolactone scaffolds using a sacrificial compression-molding process. *J Biomed Mater Res B Appl Biomater* 2006;77:287–95. doi:10.1002/jbm.b.30419.
- [4] Rai B, Lin JL, Lim ZXH, Guldberg RE, Hutmacher DW, Cool SM. Differences between in vitro viability and differentiation and in vivo bone-forming efficacy of human mesenchymal stem cells cultured on PCL-TCP scaffolds. *Biomaterials* 2010;31:7960–70. doi:10.1016/j.biomaterials.2010.07.001.
- [5] Schlichting K, Schell H, Kleemann RU, Schill A, Weiler A, Duda GN, et al. Influence of scaffold stiffness on subchondral bone and subsequent cartilage regeneration in an ovine model of osteochondral defect healing. *Am J Sports Med* 2008;36:2379–91. doi:10.1177/0363546508322899.
- [6] Lohfeld S, Cahill S, Barron V, McHugh P, Dürselen L, Kreja L, et al. Fabrication, mechanical and in vivo performance of polycaprolactone/tricalciumphosphate composite scaffolds. *Acta Biomater* 2012;8:3446–56. doi:10.1016/j.actbio.2012.05.018.
- [7] Ilizarov G. Clinical application of the tension-stress effect for limb lengthening. *Clin Orthop Relat Res* 1990;250:8–26.
- [8] Boerckel J, Kolambkar Y, Stevens H, Lin A, Dupont K, Guldberg R. Effects of in vivo mechanical loading on large bone defect regeneration. *J Orthop Res* 2012;30:1067–75. doi:10.1002/jor.22042.Effects.
- [9] Mehta M, Checa S, Lienau J, Hutmacher D, Duda GN. In vivo tracking of segmental bone defect healing reveals that callus patterning is related to early mechanical stimuli. *Eur Cell Mater* 2012;24:358–71.
- [10] Gao J, Gong H, Huang X, Fang J, Zhu D, Fan Y. Relationship between microstructure, material distribution, and mechanical properties of sheep tibia during fracture healing process. *Int J Med Sci* 2013;10:1560–9. doi:10.7150/ijms.6611.
- [11] Shefelbine SJ, Simon U, Claes L, Gold A, Gabet Y, Bab I, et al. Prediction of fracture callus mechanical properties using micro-CT images and voxel-based finite element analysis. *Bone* 2005;36:480–8. doi:10.1016/j.bone.2004.11.007.

- [12] Vijayakumar V, Marks L, Bremmer-Smith A, Hardy J, Gardner T. Load transmission through a healing tibial fracture. *Clin Biomech* 2006;21:49–53. doi:10.1016/j.clinbiomech.2005.08.011.
- [13] Roshan-Ghias A, Lambers FM, Gholam-Rezaee M, Müller R, Pioletti DP. In vivo loading increases mechanical properties of scaffold by affecting bone formation and bone resorption rates. *Bone* 2011;49:1357–64. doi:10.1016/j.bone.2011.09.040.
- [14] Taylor WR, Ehrig RM, Heller MO, Schell H, Seebeck P, Duda GN. Tibio-femoral joint contact forces in sheep. *J Biomech* 2006;39:791–8. doi:10.1016/j.jbiomech.2005.02.006.
- [15] Vayron R, Barthel E, Mathieu V, Soffer E, Anagnostou F, Haiat G. Nanoindentation measurements of biomechanical properties in mature and newly formed bone tissue surrounding an implant. *J Biomech Eng* 2012;134:021007. doi:10.1115/1.4005981.
- [16] Manjubala I, Liu Y, Epari DR, Roschger P, Schell H, Fratzl P, et al. Spatial and temporal variations of mechanical properties and mineral content of the external callus during bone healing. *Bone* 2009;45:185–92. doi:10.1016/j.bone.2009.04.249.
- [17] Steiner M, Claes L, Simon U, Ignatius A, Wehner T. A computational method for determining tissue material properties in ovine fracture calluses using electronic speckle pattern interferometry and finite element analysis. *Med Eng Phys* 2012;34:1521–5. doi:10.1016/j.medengphy.2012.09.013.
- [18] Skaggs D, Leet A, Money M, Shaw B, Hale J, Tolo V. Secondary fractures associated with external fixation in pediatric femur fractures. *J Pediatr Orthop* 1999;19:582–6.
- [19] Fischgrund J, Paley D, Suter C. Variables affecting time to bone healing during limb lengthening. *Clin Orthop Relat Res* 1994;301:31–7.
- [20] Song H, Oh C, Mattoo R, Park B, Kim S, Park I, et al. Femoral lengthening over an intramedullary nail using the external fixator: risk of infection and knee problems in 22 patients with a follow-up of 2 years or more. *Acta Orthop* 2005;76:245–52.
- [21] Zhao L, Fan Q, Venkatesh KP, Park MS, Song HR. Objective guidelines for removing an external fixator after tibial lengthening using pixel value ratio: a pilot study. *Clin Orthop Relat Res* 2009;467:3321–6. doi:10.1007/s11999-009-1011-7.
- [22] Hazra S, Song H-R, Biswal S, Lee S-H, Lee SH, Jang K-M, et al. Quantitative assessment of mineralization in distraction osteogenesis. *Skeletal Radiol* 2008;37:843–7. doi:10.1007/s00256-008-0495-7.
- [23] Song S-H, Agashe M, Kim T-Y, Sinha S, Park Y-E, Kim S-J, et al. Serial bone mineral density ratio measurement for fixator removal in tibia distraction osteogenesis and need of a supportive method using the pixel value ratio. *J Pediatr Orthop B* 2012;21:137–45. doi:10.1097/BPB.0b013e32834f04f3.

- [24] Kokoroghiannis C, Charopoulos I, Lyritis G, Raptou P, Karachalios T, Papaioannou N. Correlation of pQCT bone strength index with mechanical testing in distraction osteogenesis. *Bone* 2009;45:512–6. doi:10.1016/j.bone.2009.05.021.
- [25] Lind PM, Lind L, Larsson S, Orberg J. Torsional testing and peripheral quantitative computed tomography in rat humerus. *Bone* 2001;29:265–70.
- [26] Jamsa T, Jalovaara P, Peng Z, Ams TJ, Tuukkanen J. Comparison of Three-Point Bending Test and Peripheral. *Bone* 1998;23:155–61.
- [27] ISO. Implants for surgery - Determination of bending strength and stiffness of bone plates. ISO 95851990 1990.
- [28] Lohfeld S, Cahill S, Doyle H, McHugh P. Improving the Finite Element Model Accuracy of Tissue Engineering Scaffolds Produced by Selective Laser Sintering. *J Mater Sci Mater Med* 2015. doi:10.1007/s10856-014-5376-0.
- [29] Doyle H, Lohfeld S, McDonnell P, McHugh P. Evaluation of a multiscale modelling methodology to predict the mechanical properties of PCL/ $\beta$ -TCP sintered scaffold materials. *Ann Biomed Eng* 2014. doi:10.1007/s10439-014-1199-x.
- [30] Doyle H, Lohfeld S, McHugh P. Predicting the elastic properties of selective laser sintered PCL/ $\beta$ -TCP bone scaffold materials using computational modelling. *Ann Biomed Eng* 2014;42:661–77. doi:10.1007/s10439-013-0913-4.
- [31] Doyle H, Lohfeld S, McHugh P. Evaluating the effect of increasing ceramic content on the mechanical properties , material microstructure and degradation of selective laser sintered polycaprolactone/ $\beta$  -tricalcium phosphate materials . *Manuscr Submitt* 2014.
- [32] Bergmann G, Deuretzbacher G, Heller M, Graichen F, Rohlmann A, Strauss J, et al. Hip contact forces and gait patterns from routine activities. *J Biomech* 2001;34:859–71.
- [33] Wang C, Zhou X, Wang M. Influence of sintering temperatures on hardness and Young's modulus of tricalcium phosphate bioceramic by nanoindentation technique. *Mater Charact* 2004;52:301–7. doi:10.1016/j.matchar.2004.06.007.
- [34] Claes LE, Heigele CA. Magnitudes of local stress and strain along bony surfaces predict the course and type of fracture healing. *J Biomech* 1999;32:255–66.
- [35] Hori RY, Lewis JL. Mechanical properties of the fibrous tissue found at the bone-cement interface following total joint replacement. *J Biomed Mater Res Part A* 1982;16:911–27.
- [36] Malizos KN, Papachristos A a, Protopappas VC, Fotiadis DI. Transosseous application of low-intensity ultrasound for the enhancement and monitoring of fracture healing process in a sheep osteotomy model. *Bone* 2006;38:530–9. doi:10.1016/j.bone.2005.10.012.

- [37] Kemper A, McNally C, Kennedy E, Manoogian S, Tech V, Forest W, et al. The material properties of human tibia cortical bone in tension and compression: implications for the tibia index. Proc. 20th Enhanc. Saf. Veh. Conf., 2007.
- [38] Eshraghi S, Das S. Micromechanical finite-element modeling and experimental characterization of the compressive mechanical properties of polycaprolactone-hydroxyapatite composite scaffolds prepared by selective laser sintering for bone tissue engineering. *Acta Biomater* 2012;8:3138–43. doi:10.1016/j.actbio.2012.04.022.
- [39] Metsger DS, Rieger MR, Foreman DW. Mechanical properties of sintered hydroxyapatite and tricalcium phosphate ceramic. *J Mater Sci Mater Med* 1999;10:9–17.
- [40] Boilet L, Descamps M, Rguiti E, Tricoteaux A, Lu J, Petit F, et al. Processing and properties of transparent hydroxyapatite and  $\beta$  tricalcium phosphate obtained by HIP process. *Ceram Int* 2013;39:283–8. doi:10.1016/j.ceramint.2012.06.023.

## 9 Tables and Figures

**Table 1:** List of mechanical properties, elastic modulus ( $E$ ) and Poisson's ratio ( $\nu$ ), for tibial callus defect simulations (bending and compression).

<b>Material</b>		<b><math>E</math> (MPa)</b>	<b><math>\nu</math></b>	<b>Reference</b>
$\beta$ -TCP Scaffold		$24.6 \times 10^3$	0.3	[33]
90/10wt% PCL/ $\beta$ -TCP Scaffold	Undegraded	250.37	0.3	[29]
	Degraded	93.71	0.3	[31]
Cortical Bone		$11 \times 10^3$	0.3	Section 3.4, [34]
Soft Tissue		2	0.167	[35]
Callus Tissues (Models with $\beta$ -TCP Scaffolds)	Range 1	$1 \times 10^3$	0.3	Upper and lower values reported in [34]
	Range 2	$2.23 \times 10^3$	0.3	
	Range 3	$3.61 \times 10^3$	0.3	
	Range 4	$4.76 \times 10^3$	0.3	
	Range 5	$6 \times 10^3$	0.3	
Callus Tissues (Models with PCL/ $\beta$ -TCP Scaffolds)	Range 1	630.42	0.3	Based on results from values reported in [34], scaled as per Section 3.4
	Range 2	$1.43 \times 10^3$	0.3	
	Range 3	$2.21 \times 10^3$	0.3	
	Range 4	$3 \times 10^3$	0.3	
	Range 5	$3.78 \times 10^3$	0.3	

**Table 2:** Summary of values for elastic modulus ( $E$ ) and ultimate strength ( $\sigma_U$ ) for each material as used in Section 3.6.

<b>Material</b>	<b><math>\sigma_{UC}</math> (MPa)</b>	<b><math>\sigma_{UT}</math> (MPa)</b>	<b>Notes</b>
Callus Tissue	17.7*	14.6 [36]	*Evaluated based on ratio of 1.21 [37] between $\sigma_{UC}$ and $\sigma_{UT}$ for cortical bone.
90/10wt% PCL/ $\beta$ -TCP Scaffold	33.7* [38]	2.01 [31]	*Data for this material was unavailable; this value was evaluated for a 90/10wt% PCL/hydroxyapatite solid cylinder fabricated using SLS
$\beta$ -TCP	315 [39]	181 [40]	*Evaluated using 3-pt Bending

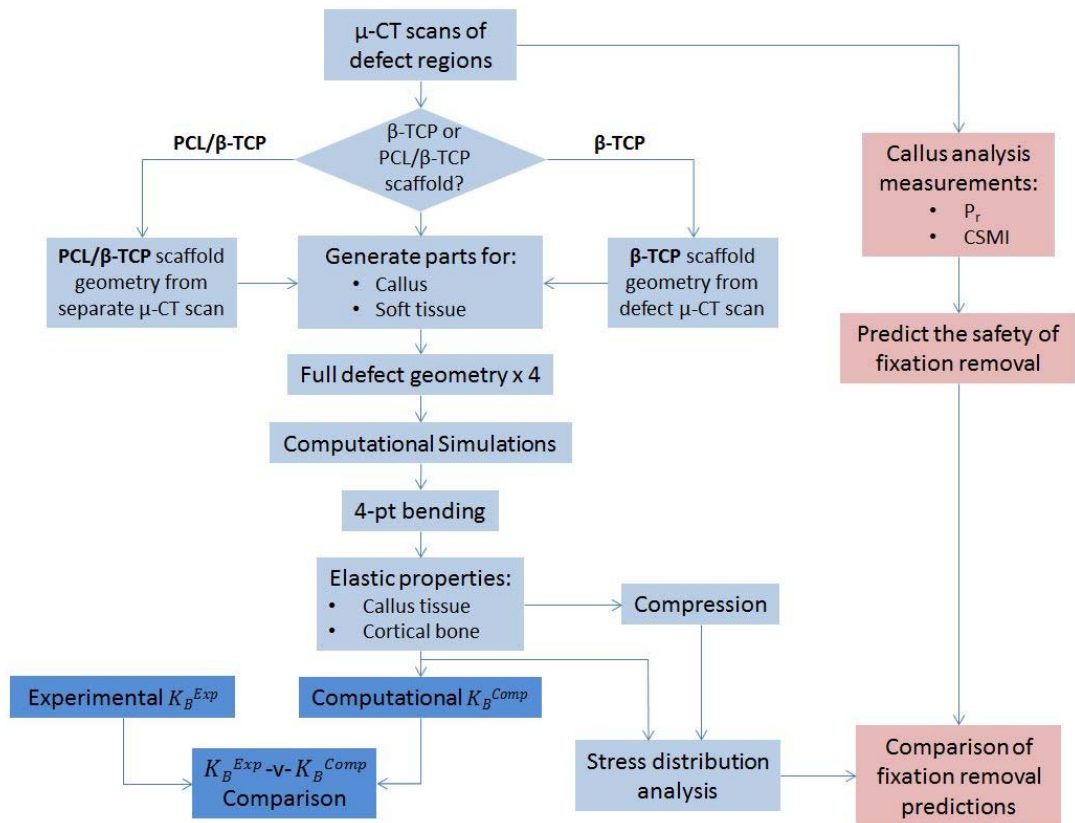


**Figure 1:** Flowchart outlining the individual steps in this study for the case of PCL/ $\beta$ -TCP scaffolds and of  $\beta$ -TCP scaffolds.

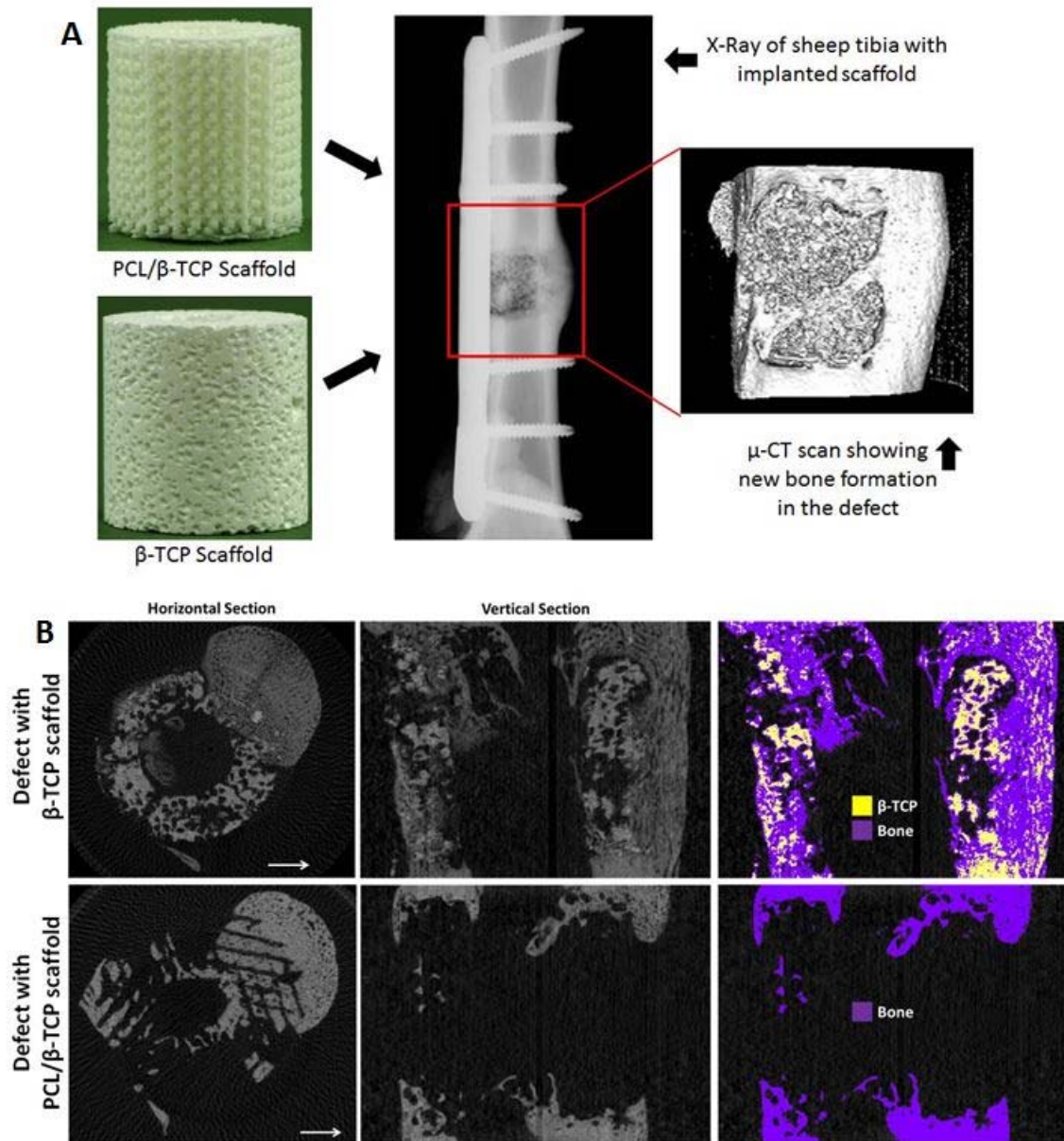


**Figure 2:** PCL/β-TCP scaffolds and β-TCP scaffolds were implanted in critical-sized defects in ovine tibiae as part of the STEPS EU-FP6 project [6] (A). Sections of μ-CT scans of *in-vivo* callus with an implanted β-TCP and PCL/β-TCP scaffolds are shown in (B): (L-R) horizontal section, vertical section and vertical section showing new bone formation (purple) and regions of high density indicating scaffold location for β-TCP scaffolds (yellow). Note that the scaffold is not visible in the defect with an implanted PCL/β-TCP scaffold due to low density relative to that of bone.

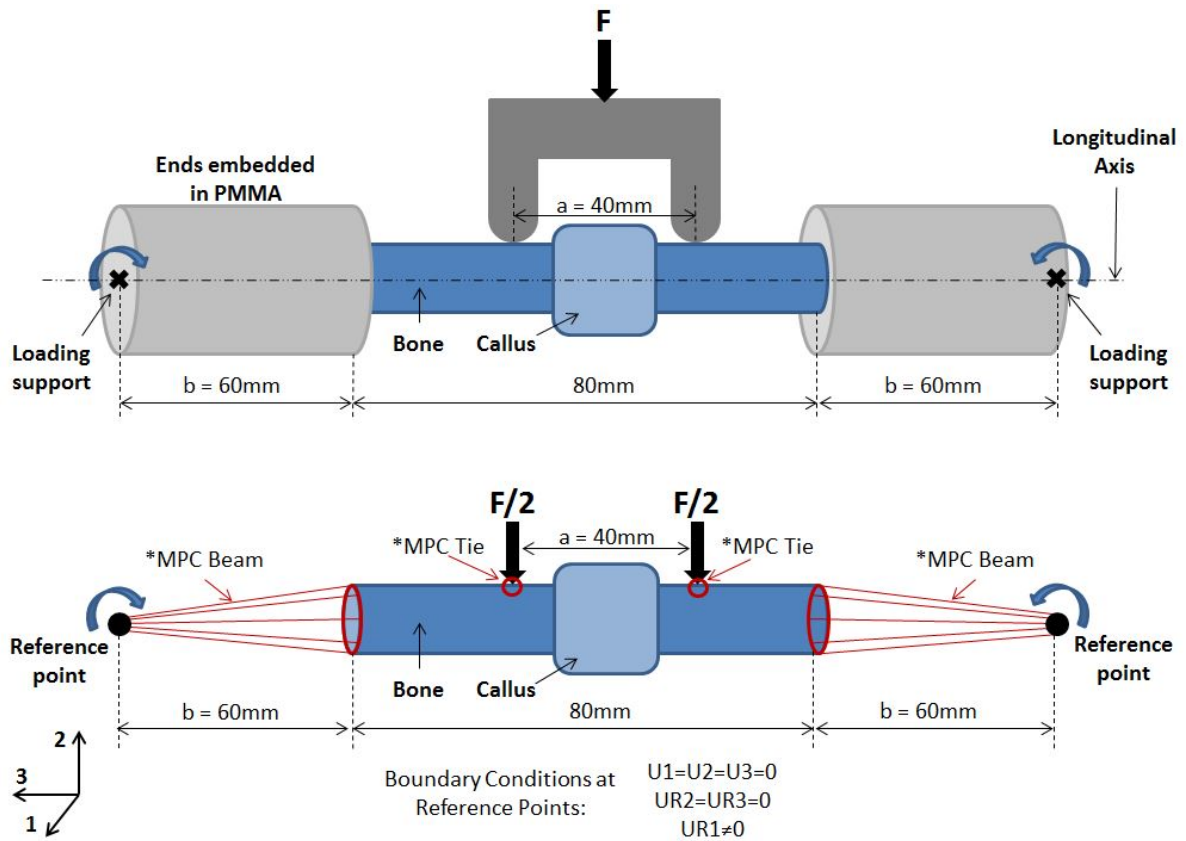


**Figure 3:** Schematic diagram of the experimental four-point bending test set-up (A) used to evaluate tibial bending stiffness by Lohfeld et al. [6], and of the computational model implementation of the four-point bending set-up (B).

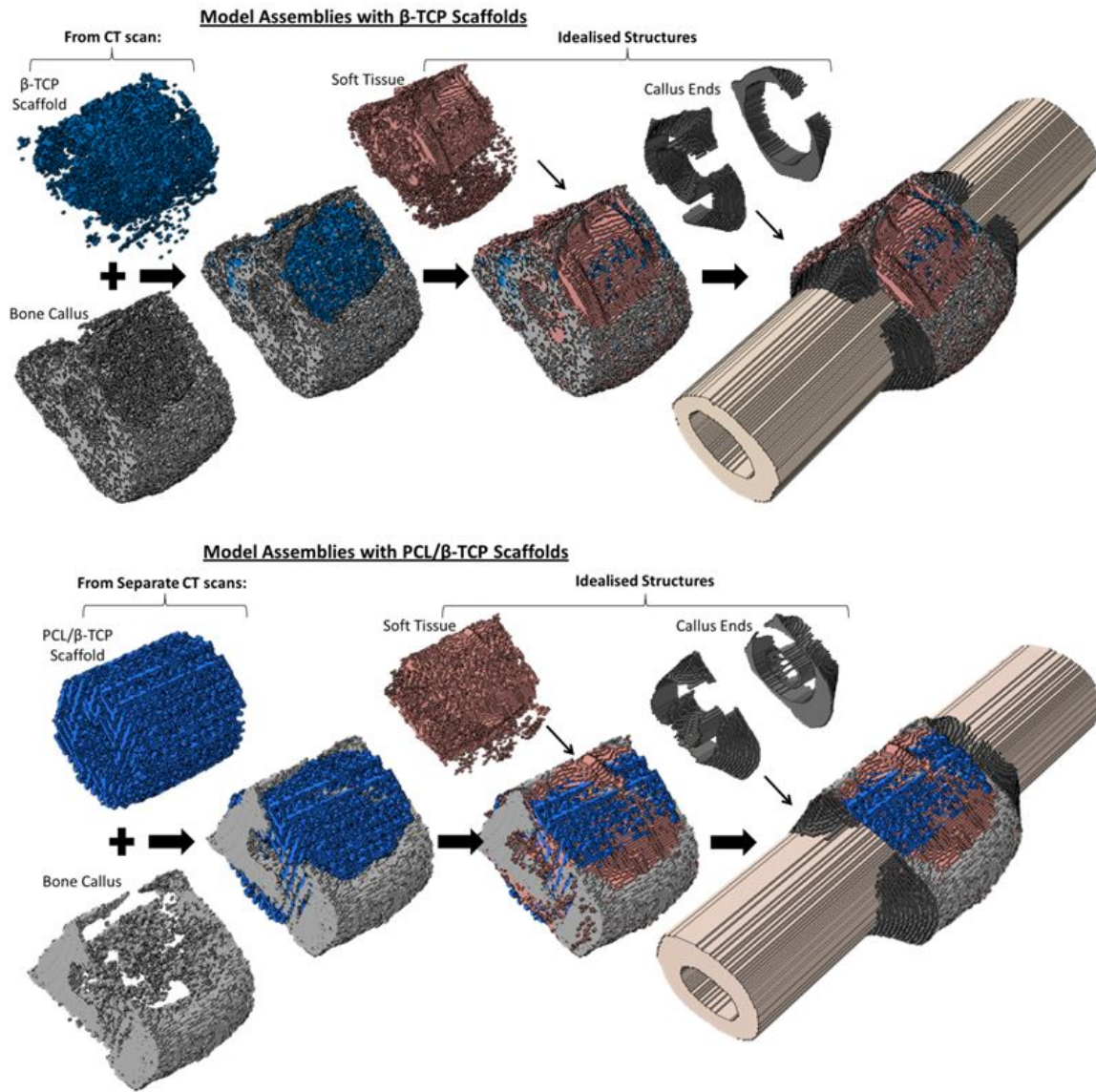


**Figure 4:** Schematic diagram illustrating the assembly of model geometries for tibial defects with  $\beta$ -TCP scaffolds (top) and with PCL/ $\beta$ -TCP scaffolds (bottom). For defects with  $\beta$ -TCP scaffolds, the scaffold and bone callus geometries are obtained directly from one  $\mu$ -CT scan. For defects with PCL/ $\beta$ -TCP scaffolds, the scaffold geometry is obtained from a separate  $\mu$ -CT scan from the bone callus, and is carefully positioned to fit the regions containing scaffold struts visible in bone callus scan images. In both cases the soft tissue and callus ends parts are idealised structures generated based on the  $\mu$ -CT scan geometries.

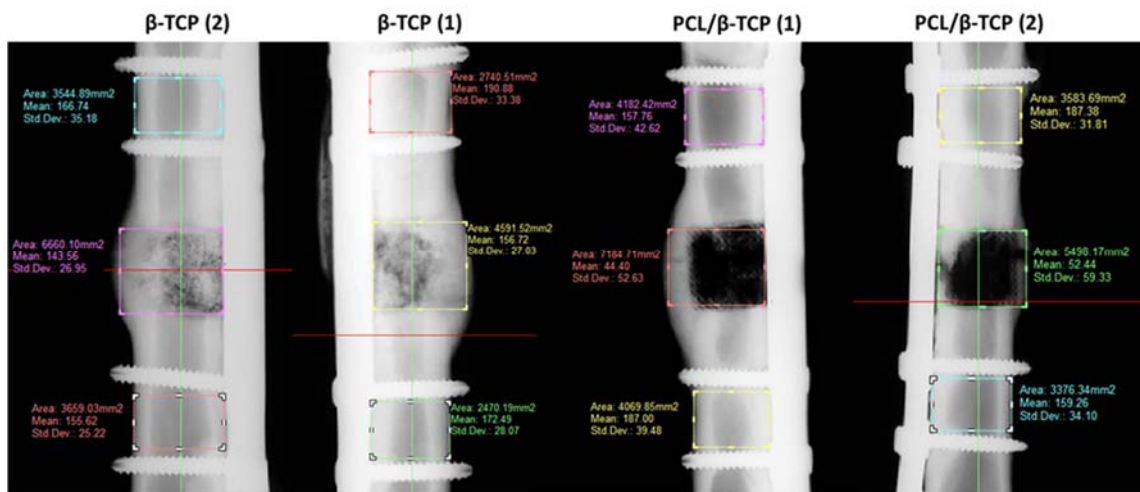


**Figure 5:** Evaluation of regional average pixel values for the calculation of pixel ratio values for each defect.

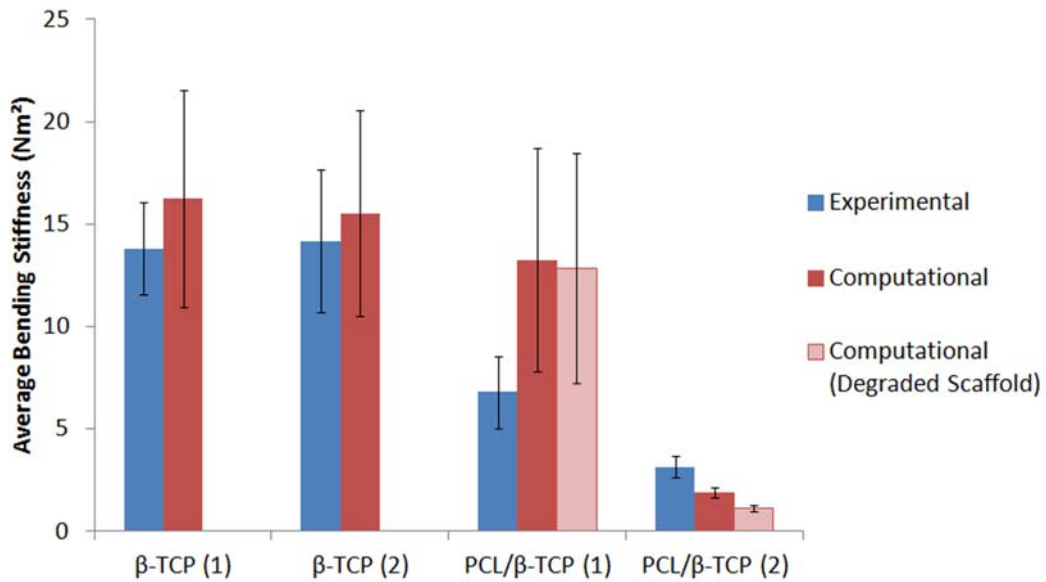


**Figure 6:** Bending stiffness calculated from four-point bending simulations of tibial defects (red). Data for simulations using degraded PCL/β-TCP scaffold elastic modulus values (pink) are also included. Experimentally-evaluated average bending stiffness for each specific tibial defect (blue), evaluated from data generated in a previous study [6], are included for comparison purposes. Mean values for each data set are shown and error bars represent standard deviation.

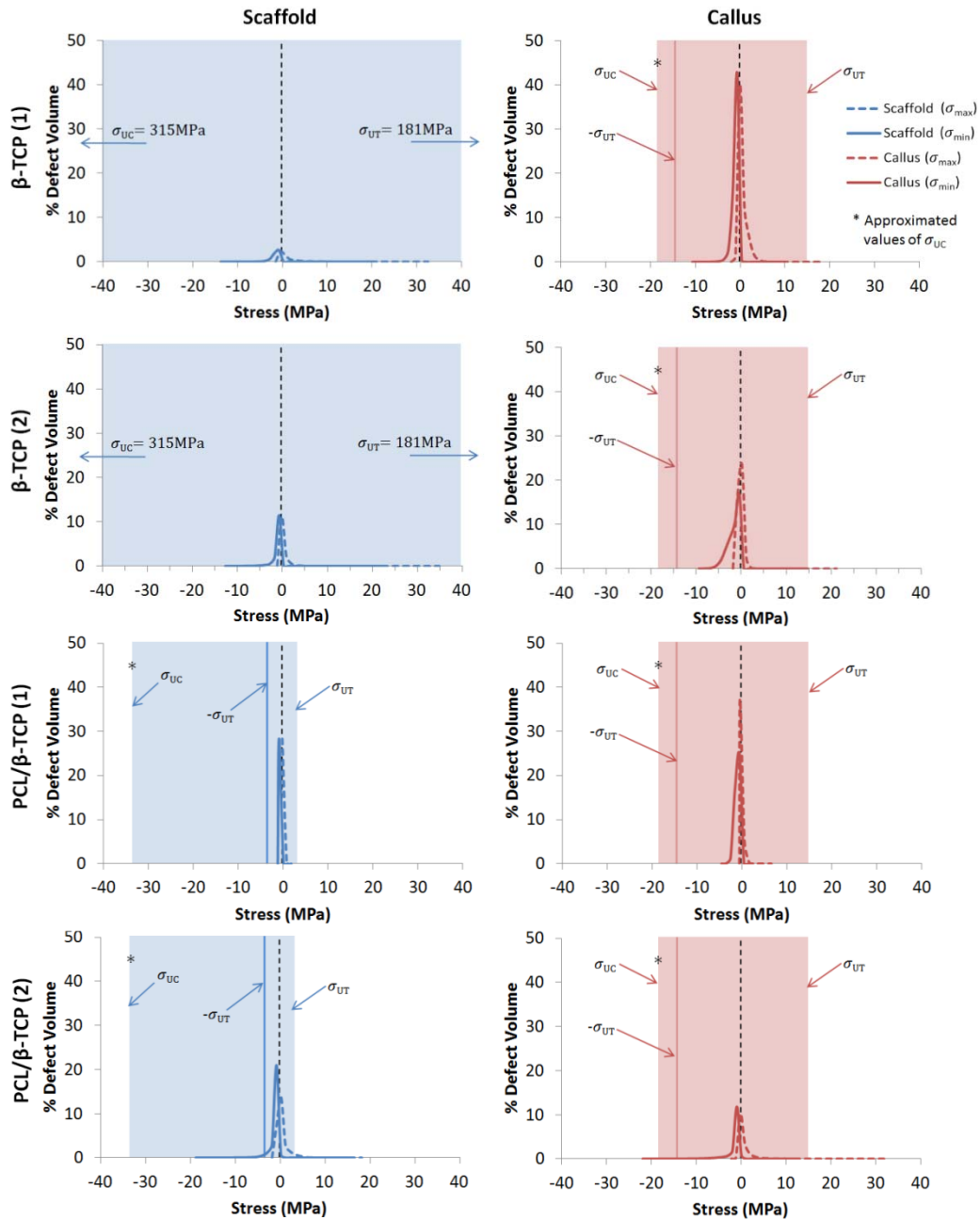


**Figure 7:** Principal stress distributions for four-point bending simulations of tibiae with scaffolds and defects. The shaded regions represent stresses between the compression and tensile ultimate strength values ( $\sigma_{UC}$ ,  $\sigma_{UT}$ ) of the scaffold materials (blue) and callus tissue (red). An asterisk (\*) indicates values of  $\sigma_{UC}$  that are approximated from the literature. Solid lines indicating values of  $-\sigma_{UT}$  are included to indicate conservative values of ultimate compressive strength.

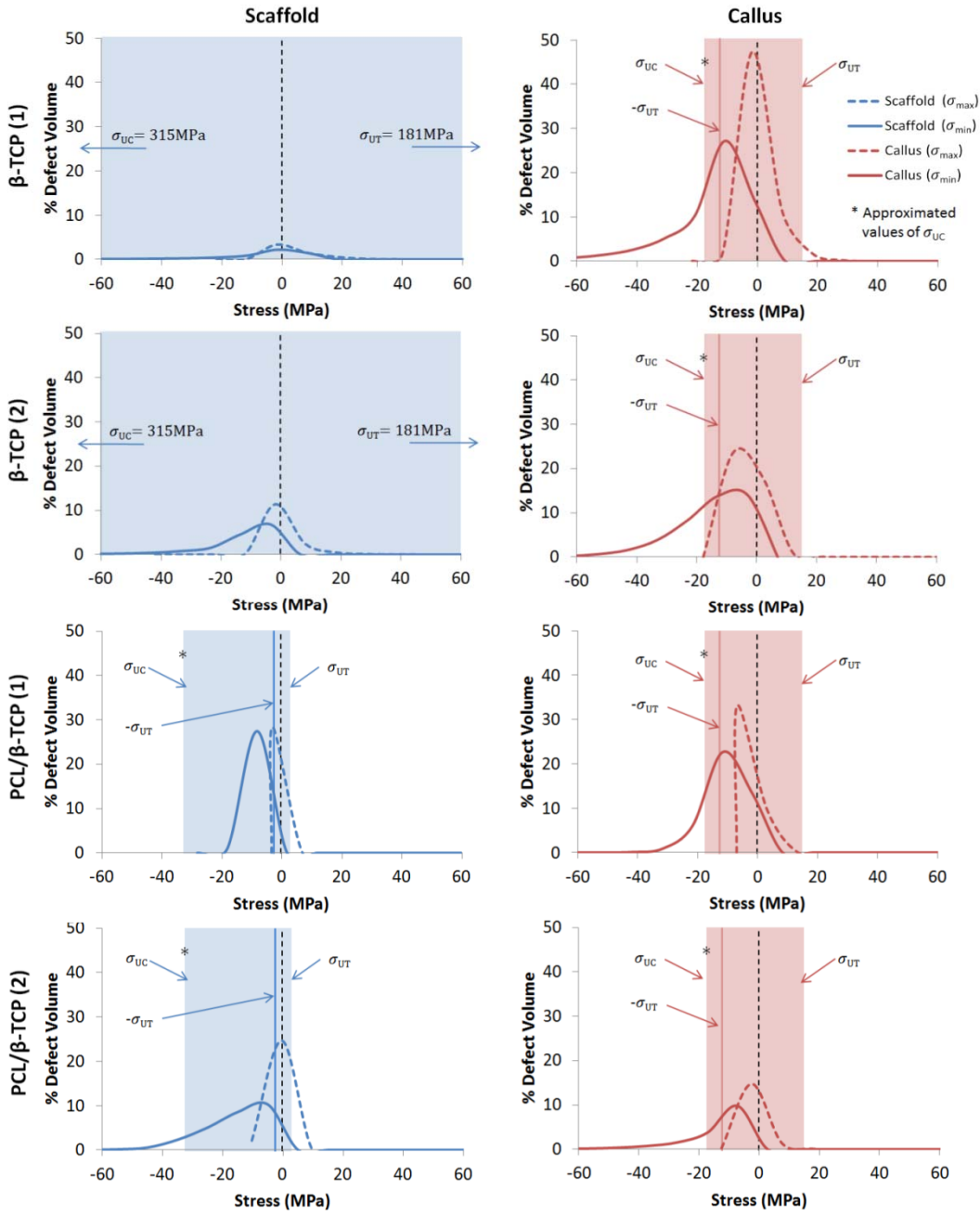


**Figure 8:** Principal stress distribution for compression simulations of tibiae with scaffolds and defects. The shaded regions represent stresses between the compression and tensile ultimate strength values ( $\sigma_{UC}$ ,  $\sigma_{UT}$ ) of the scaffold materials (blue) and callus tissue (red). An asterix (\*) indicates values of  $\sigma_{UC}$  that are approximated from the literature. Solid lines indicating values of  $-\sigma_{UT}$  are included to indicate conservative values of ultimate compressive strength.

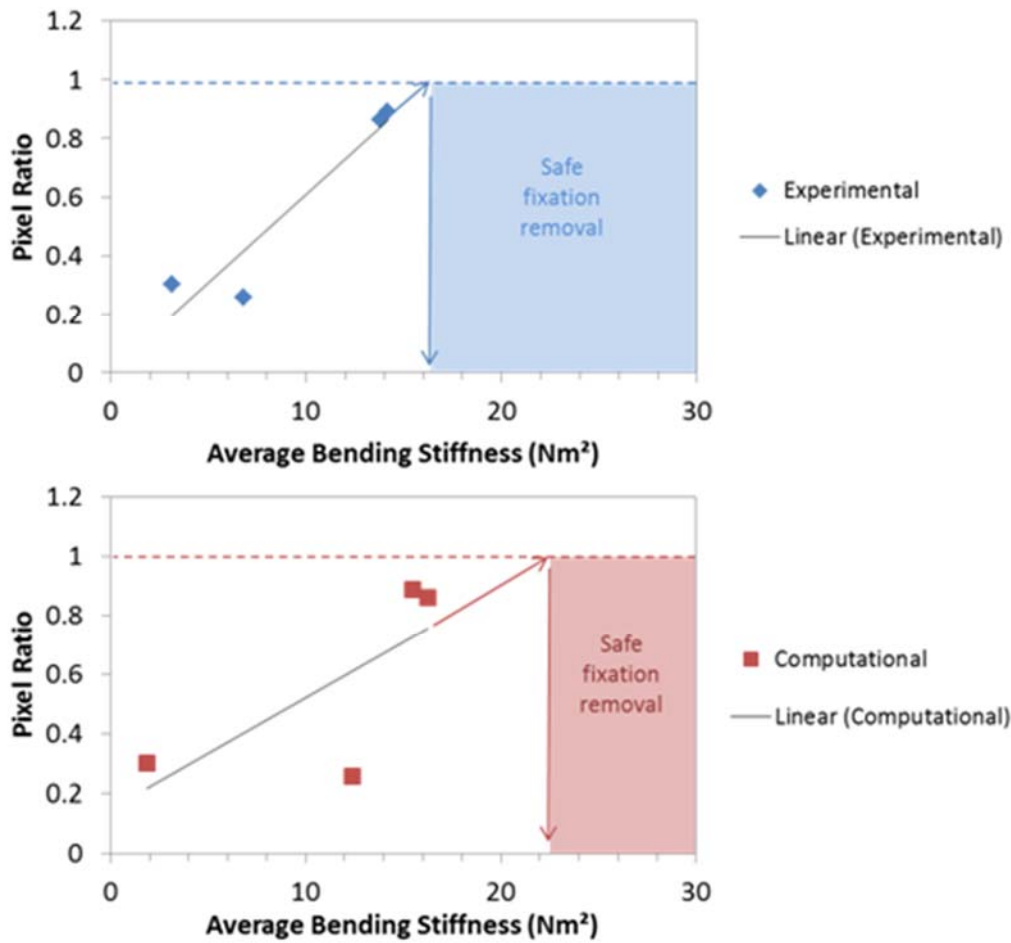


**Figure 9:** Pixel ratio ( $P_r$ ) versus average bending stiffness for experimentally evaluated bending stiffness (above, blue) and computationally evaluated bending stiffness (below, red). A pixel ratio value of 1 has been suggested for safe fixation removal. A linear fit is shown for each data set, and is used to determine the value of average bending stiffness corresponding to a pixel ratio value of 1 for safe fixation removal. Values of 16.5 and 22.7 Nm<sup>2</sup> were determined from the experimental and computational data sets, respectively.

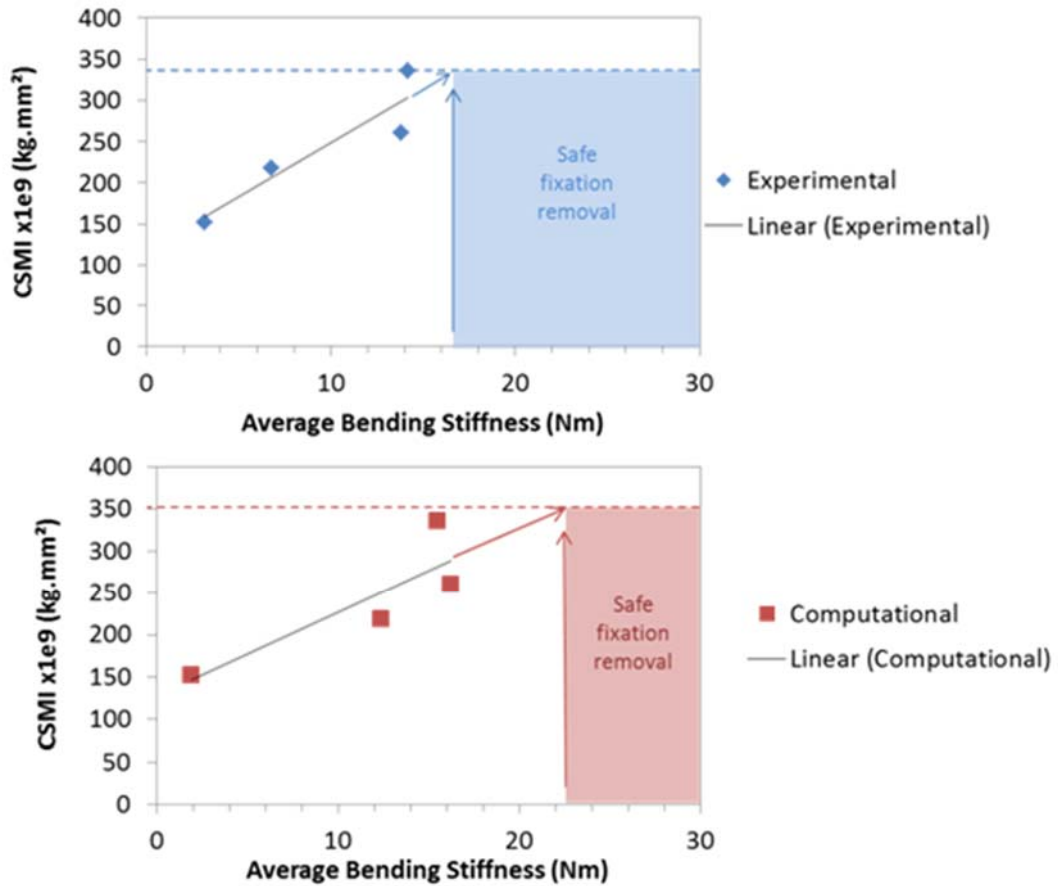


**Figure 10:** Cross-sectional moment of inertia (*CSMI*) versus average bending stiffness for experimentally evaluated bending stiffness (above, blue) and computationally evaluated bending stiffness (below, red). Average bending stiffness values of 16.5 and 22.7 Nm<sup>2</sup> for safe fixation removal were determined for the experimental and computational data sets, respectively from Figure 9. A linear fit is shown for each data set, and is used to determine corresponding values of *CSMI* for safe fixation removal, giving values of 334x10<sup>9</sup> Nm<sup>2</sup> and 353x10<sup>9</sup> Nm<sup>2</sup> for the experimental and computational data sets, respectively.